Laser & Photonics Reviews

www.lpr-journal.org

RESEARCH ARTICLE

Engineering Integral and Differential Dispersion With Subwavelength-Scaled Planar Metastructures for Image Encryption

Hanfei Bu[1] | Pengyu Fu[1] | Yue Li[1,2,3]

[1]Department of Electronic Engineering, Tsinghua University, Beijing, China | [2]Beijing National Research Center for Information Science and Technology, Beijing, China | [3]State Key Laboratory of Space Network and Communications, Beijing, China

Correspondence: Yue Li (lyee@tsinghua.edu.cn)

Received: 13 September 2025 | **Revised:** 27 November 2025 | **Accepted:** 3 December 2025

Keywords: epsilon-near-zero | image encryption | optical analog computing | planar metastructure

ABSTRACT

Optical analog computing offers inherent advantages such as ultrahigh computational density and minimal power consumption, yet practical deployment remains limited by bulky and fabrication-intensive architectures. Inspired by the ability of epsilon-near-zero (ENZ) materials to manipulate dispersion within a subwavelength scale, we propose a planar pixel metastructure strategy that emulates and tailors such compact dispersion responses within a fully planar, fabrication-compatible architecture. Instead of employing lossy plasmonic materials or complex three-dimensional (3D) waveguide effective ENZ media, the reconfigurable pixelated architecture allows deterministic dispersion engineering at the subwavelength scale, enabling compact and integrable pixel metastructure processing units (pixel-MPUs). As a proof of concept, we design and experimentally verify pixel-MPUs that realize integration and differentiation functions, and further demonstrate real-time image encryption and decryption using cascaded operators with negligible latency and energy consumption. The proposed pixel-MPUs combine functionality, scalability, and broad planar-process compatibility, providing a practical foundation for highly integrated and manufacturable optical analog computing systems.

1 | Introduction

Digital electronic architectures have powered information processing for decades, but are increasingly strained by emerging workloads. For example, modern artificial intelligence (AI) applications have grown so computationally intensive that conventional hardware struggles to meet their throughput and energy-efficiency demands [1–3]. Similarly, proof-of-work blockchain protocols and high-security encryption require massive computation, further pushing digital systems toward the limits of Moore's Law [4–9]. These challenges motivate the exploration of alternatives beyond purely digital processors. Analog computing, especially in the optical domain, is re-emerging as a promising paradigm [10–13], offering ultra-high throughput and intrinsically low power consumption [14–20]. By allowing mathematical operations such as differentiation, integration, and convolution to be performed directly in the wave domain [21–25], optical analog computing circumvents digital overheads such as quantization, clocked logic, and analog-to-digital conversion, making it especially suitable for real-time applications. For instance, photonic neural networks based on Mach–Zehnder interferometer (MZI) meshes have demonstrated orders-of-magnitude improvements in computing speed and energy efficiency compared to electronic counterparts [26–28]. Likewise, dielectric metasurfaces have been experimentally shown to execute spatial derivatives and real-time image edge detection fully optically [29–31], and inverse-

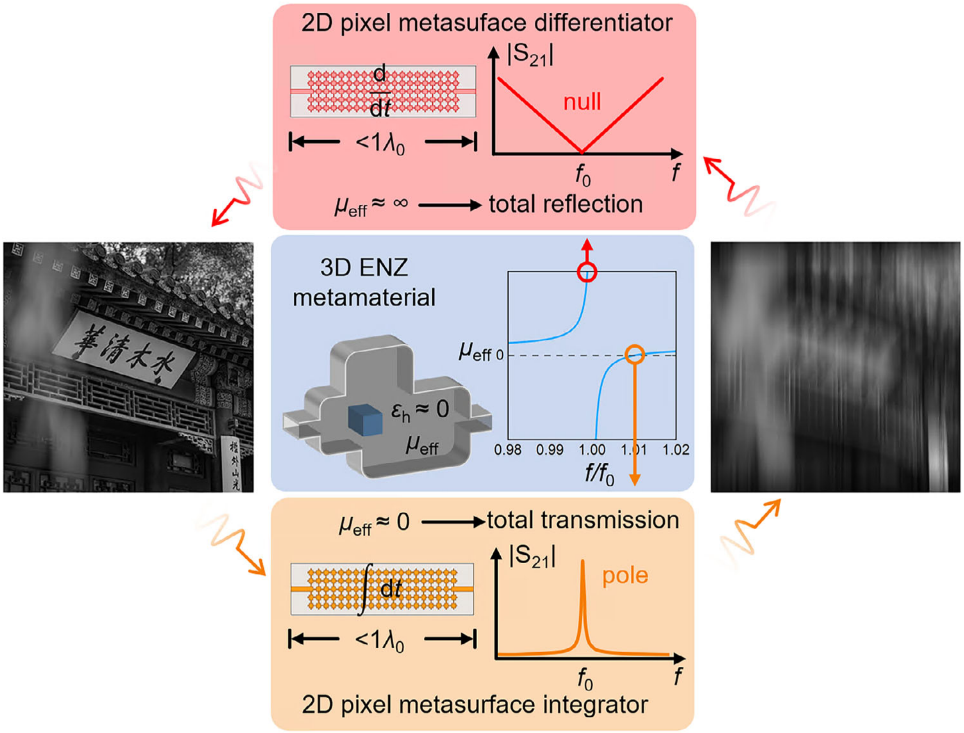

FIGURE 1 | Conceptual framework of dispersion-engineered 2D pixel metastructures for analog image encryption. 3D ENZ metamaterials can efficiently tune μ_{eff} through doping, thereby realizing transmission zeros and poles corresponding to differentiation and integration operations. Planar pixel metastructures can emulate ENZ dispersion by spatially tailoring meta-atoms, enabling the same functionalities within planar subwavelength-scale structures. This figure illustrates the schematic of real-time image encryption and decryption using the pixel-MPU integrator-differentiator pair.

designed metamaterials can even solve linear calculus equations [32]. Despite all the advantages, most existing optical analog computing platforms suffer from bulky free-space optics and limited compatibility [33, 34] with modern planar microelectronic systems, which severely restricts their scalability [35], integration density, and practical deployment [36].

Beyond device-level architectures, the choice of material platform has also become increasingly crucial for enabling high-density optical analog computing. Among the candidates, epsilon-near-zero (ENZ) metamaterials have emerged as a particularly promising physics platform due to their unusual dispersion characteristics [37–39]. In ENZ media, the effective permittivity approaches zero, allowing electromagnetic waves to experience extremely large effective wavelength, enabling deeply subwavelength dispersion engineering [40–44]. Unlike conventional photonic devices that rely on modal interference or resonance, ENZ systems exploit dispersion-driven transmission poles and zeros for compact analog signal processing [45]. However, their narrow bandwidth and the fabrication complexity of 3D metastructures limit on-chip scalability, motivating alternatives that maintain ENZ-like dispersion tunability while enabling planar, high-density integration.

In this work, we introduce a paradigm shift by using two-dimensional (2D) pixel metastructures to realize highly tailorable subwavelength dispersion engineering inspired by the dispersion characteristics commonly associated with ENZ media. A schematic overview of this concept is provided in Figure 1. Rather than relying on bulky 3D architectures or lossy plasmonic materials, our approach leverages spatially varying meta-atoms to flexibly manipulate the dispersion profile within a planar, low-loss footprint. As a proof of concept, we implement integrators and differentiators, showing that the pixel metastructure platform can be reconfigured to realize distinct transfer functions. These 2D pixel metastructure processing units (pixel-MPUs) operate directly on time-varying optical fields, enabling instantaneous mathematical operations such as integration and differentiation with low latency and minimal power consumption. To support these capabilities, we develop a physics-informed optimization framework that maps arbitrary target transfer functions onto manufacturable pixel layouts, further highlighting the flexibility of our dispersion-engineering strategy. By harnessing the reconfigurable nature of pixel metastructures, the proposed pixel-MPUs overcome the integration and fabrication constraints of ENZ-based implementations and offer a scalable route to customized on-chip analog computing. More broadly, this work establishes a compact and energy-efficient platform suitable for edge computing and secure communication scenarios where integration density and real-time processing are essential.

2 | Results

2.1 | Inverse-Designed Pixel-MPUs With Engineered ENZ Dispersion

Dispersion-based optical encryption and decryption using ENZ-inspired pixel metastructures are illustrated in Figure 1. The input image is first unwrapped column-wise into a 1D temporal sequence, $h(t)$, which is then encrypted through an optical integration process that effectively smooths and conceals the image content. Decryption is subsequently performed via optical differentiation, exploiting the inverse relationship between differentiation and integration to realize a fully analog encryption–decryption framework for image signals. In the frequency domain, integrating $h(t)$ yields $H(\omega)/\mathrm{j}\omega$, where $H(\omega)$ denotes the Fourier transform of $h(t)$. When the signal is spectrally modulated around a center frequency ω_0 , the corresponding spectrum becomes $H(\omega-\omega_0)/\mathrm{j}(\omega-\omega_0)$, indicating the presence of a pole at ω_0. Conversely, for differentiation, the Fourier transform is $\mathrm{j}\omega H(\omega)$, which transforms into $\mathrm{j}(\omega-\omega_0)H(\omega-\omega_0)$ when centered at ω_0 . As a result, integration and differentiation yield transfer functions $T_\mathrm{d}(\omega) = \mathrm{j}(\omega-\omega_0)$ and $T_\mathrm{i}(\omega) = 1/\mathrm{j}(\omega-\omega_0)$, indicating that ideal analog calculus requires dispersive responses containing a well-placed in-band pole or zero. This formulation naturally reduces time-domain signal processing to the problem of engineering specific spectral features—namely, targeted transmission poles and zeros.

This requirement connects naturally to systems capable of shifting transmission poles and zeros through controlled dispersion. ENZ metamaterials provide one such example, as their effective permittivity can be tuned through doping or structural dispersion, enabling the placement of spectral poles and zeros that resemble those required for analog calculus. In conjunction with the Fano resonance in waveguide-based ENZ structures, ENZ metamaterial processing units (ENZ-MPUs) can approximate integrator- and differentiator-type transfer functions [46]. However, the intrinsically narrow bandwidth and multilayer complexity of ENZ implementations restrict their practical operating range to below ~15% and pose challenges for large-scale planar integration.

To overcome these limitations, we adopt a planar metastructure composed of pixelated meta-atoms. By optimizing the meta-atoms' interconnections to emulate the desired dispersive behavior, the resulting pixel-MPU establishes transmission zeros and poles within a subwavelength planar architecture, thereby realizing broadband low-loss analog differentiation and integration functionalities.

The layout of the planar pixel metastructure is shown in Figure 2a. The structure comprises an array of square metallic patches and their associated interconnecting elements. The meta-atoms on the top surface form a patterned metal layer, supporting quasi-TEM wave propagation with a continuous ground plane on the backside of the dielectric substrate. Each patch has a uniform side length w_p and is connected to its neighbors through narrow metallic strips of width w_c, which function as reconfigurable interconnections. Each strip can be set to either an ON or OFF state. In the OFF state, the strip is interrupted at its center by a slit of gap length l_c, thereby electrically isolating the adjacent patches. In both states, the strip ends are embedded into the neighboring patches over a contact length l_p, ensuring mechanical stability and well-defined current paths when connections are enabled. Two feeding lines, each of width w_p, are positioned on opposite sides of the metastructure to enable excitation and signal injection. By selectively configuring the ON/OFF states of the interconnecting strips, the electromagnetic dispersion characteristics of the metastructure can be precisely tuned, enabling programmable transfer functions between the input and output ports. To reduce the number of full-wave simulations and accelerate the inverse design process, a simplified modeling strategy based on the method of moments was employed. In this approach, each programmable strip—configured in the ON or OFF state—is modeled as an equivalent port terminated with an impedance of 0 Ω (short) or ∞ Ω (open), respectively. Under this abstraction, the entire pixel metastructure is represented as a multi-port network, where the static geometry is characterized once via a full-wave simulation, and the programmable interconnections are incorporated analytically. For a pixel metastructure comprising y rows and x columns of meta-atoms, as shown in Figure 2a, the total number of equivalent ports is given by $N = 2xy\text{-}x\text{-}y$, accounting for all possible horizontal and vertical connections between adjacent meta-atoms. The total impedance matrix Z_0 of the system is constructed from the full-wave simulation. It comprises the impedance submatrix between the two feeding ports Z_f, the impedance submatrix among the N equivalent ports Z_e, and the mutual impedance matrices between the feeding ports and the equivalent ports $Z_{f,e}$ and $Z_{e,f}$.

$$Z_0 = \begin{bmatrix} Z_f & Z_{f,e} \\ Z_{e,f} & Z_e \end{bmatrix} \tag{1}$$

Once a specific ON/OFF configuration is defined, the corresponding impedance load vector Z_L is assigned to the N equivalent ports with entries of either 0 or ∞. The effective impedance between the two feeding ports can then be calculated using the following matrix equation.

$$Z_p = Z_f - Z_{f,e}(Z_e + Z_L)^{-1} Z_{e,f} \tag{2}$$

This matrix-based formulation enables rapid evaluation of the transmission characteristics for any given strip configuration without requiring repeated electromagnetic simulations. The binary nature of the ON/OFF states defines a discrete design space, naturally framing the inverse design problem as a combinatorial optimization task. This discrete representation is well-suited for global optimization algorithms such as genetic algorithms (GA), which can efficiently search for configurations that implement desired transfer functions or dispersion profiles [47].

Figure 2b depicts the optimization framework and representative intermediate results for an integration-type pixel-MPU. Rather than adopting purely random initialization for the initial population in the GA, a physics-inspired pathway initialization strategy was adopted. This method constructs randomized conductive pathways between the input and output ports, ensuring sufficient surface-current propagation distances at subwavelength scales. Following pathway initialization, a small degree of randomness is introduced to enhance population diversity, after which a short preliminary screening is performed using a GA with a high mutation rate. This step efficiently eliminates poor candidates, such as configurations exhibiting all-pass or all-stop characteristics within the target frequency band. The remaining population then undergoes 100 iterations of final optimization using a lower mutation rate. Denoted as loss in Figure 2b, the fitness function measures the linear correlation between the dispersion curve of the current design and the target transfer function, with additional penalties for center-frequency deviation in operations

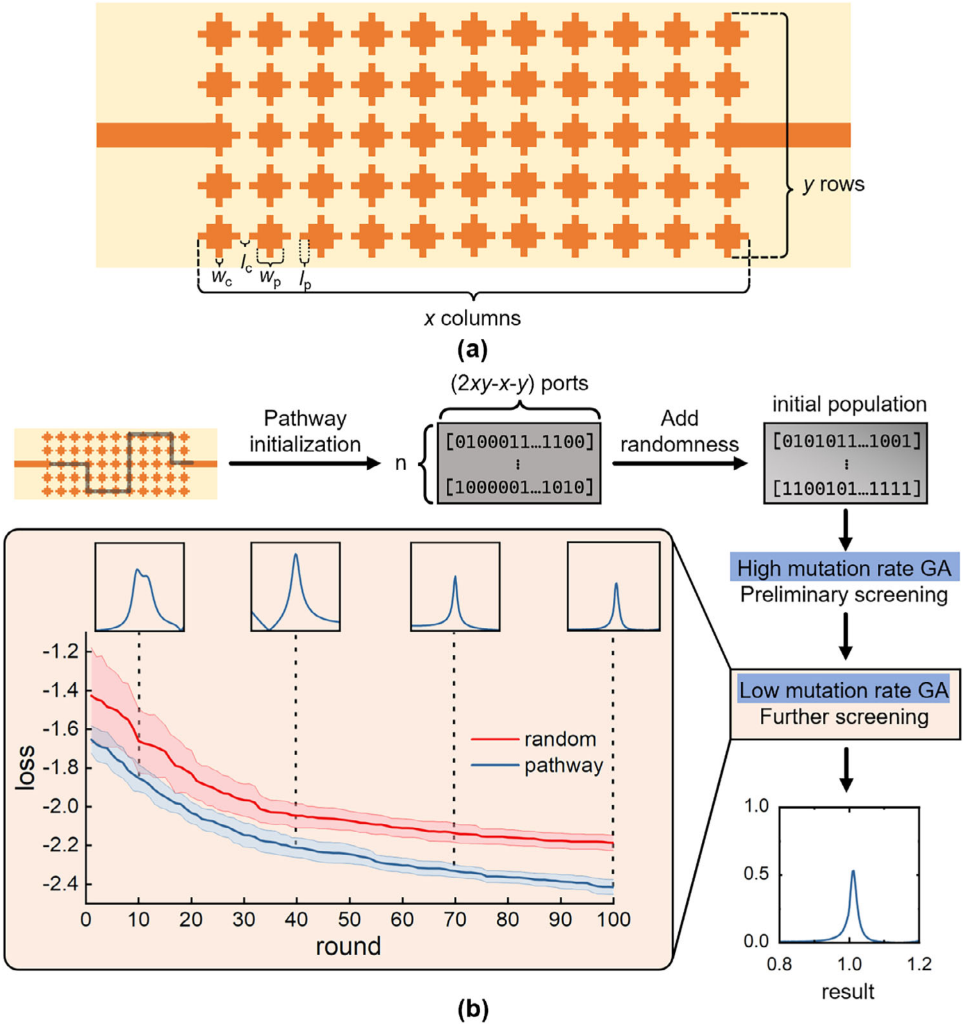

FIGURE 2 | Basic structure of pixel metastructure processor and the optimization framework. (a) Schematic of the pixel-MPU composed of x columns and y rows of meta-atoms. Adjacent patches are connected by programmable strips of width w_c, with each strip embedded into neighboring patches over a length l_p and optionally interrupted by a slit of length l_c. Feeding lines of width w_p are placed on both ends for signal injection and collection. The total number of programmable interconnections is $N = 2xy\text{-}x\text{-}y$. (b) Schematic of the physics-informed optimization workflow. A pathway initialization ensures electrical continuity between ports, followed by randomness injection and two-stage GA optimization. The bottom plot compares optimization performance between pathway and random initialization strategies. Shaded regions represent the 95% confidence interval, and insets show representative transmission spectra at selected generations.

such as differentiation or integration. As shown in Figure 2b, pathway initialization (blue curve) yields both faster convergence and superior final performance compared to random initialization (red curve). The shaded areas represent the 95% confidence intervals over more than 100 trials, and the smaller spread for pathway initialization highlights its improved robustness. Insets at selected optimization rounds (10, 40, 70, and 100) illustrate the evolution of the transmission spectra, showing that pathway-initialized designs rapidly converge toward the desired spectral profile. The 10th-iteration results confirm the effectiveness of the initial screening stage, while the progression from the 10th to the 100th iteration demonstrates that the pixel metastructure can precisely control the placement of transmission nulls and poles.

Figure 3a shows photographs of the fabricated pixel-MPU prototypes, with the integrator on the right and the differentiator on the left. For fabrication and measurement convenience, a center frequency of 1.0 GHz was selected without loss of generality. The structural parameters used are: $x = 20$, $y = 5$, $w_p = 4$ mm, $w_c = 0.8$ mm, $l_p = 1.2$ mm, and $l_c = 0.8$ mm. The structure was printed on a Rogers RO4350B substrate (relative dielectric constant $\varepsilon_r = 3.66$, loss tangent $\tan\delta = 0.002$) of 2 mm thickness. The total footprint is 175×45 mm^2, corresponding to $0.58\lambda_0 \times 0.15\lambda_0$ (λ_0 is the free-space wavelength at the center frequency) with subwavelength footprints. Sub-miniature version A (SMA) connectors were soldered to both ends of the pixel-MPUs, and transmission characteristics were measured using a vector network analyzer. The measured results show excellent agreement with simulations, with a minor deviation near the center frequency. The fabricated pixel-MPU exhibits a measured center frequency of approximately 1.01 GHz, as shown in Figure 3b–e. The integrator presents a pronounced magnitude peak at the center frequency, while the differentiator displays a deep null at the same frequency. Both devices exhibit abrupt phase transitions at the center frequency, in agreement with theoretical predictions. Moreover, they exhibit operational bandwidths exceeding 25%,

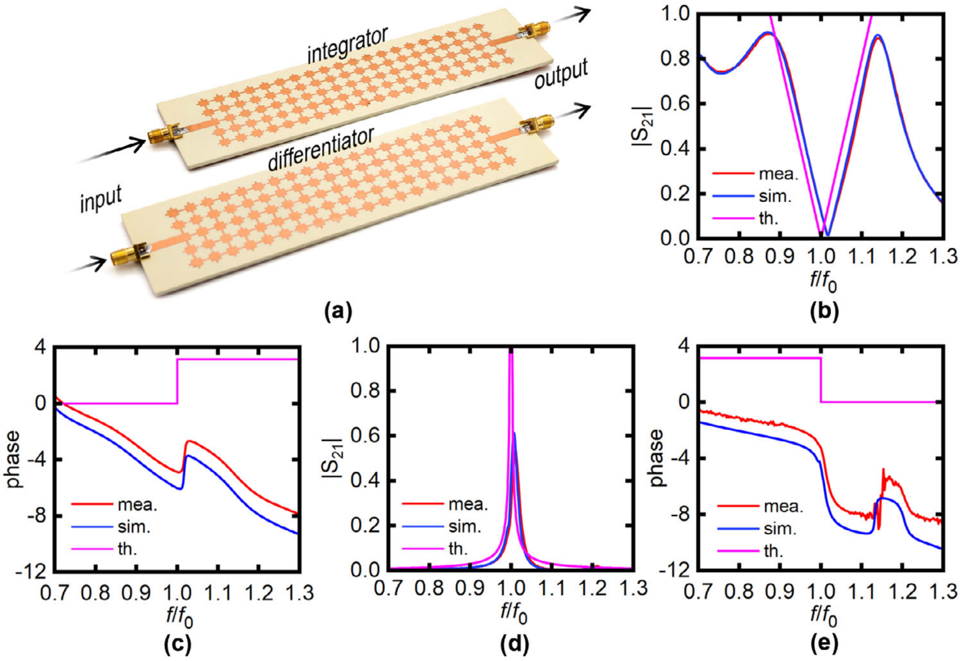

FIGURE 3 | Measured results of the differentiator and the integrator. (a) The photo of the fabricated pixel-MPU differentiator and integrator. (b) The magnitude and (c) phase of the integrator's transmission function. (d) The magnitude and (e) phase of the differentiator's transmission function.

which is much more than the ~15% bandwidth reported for the ENZ-MPUs in [45].

To further verify the functionality, a time-domain demonstration was conducted using a Gaussian pulse, as illustrated in Figure 4. The input signal was upconverted before being fed to the pixel-MPU and subsequently downconverted at the output for analysis. The normalized waveforms are presented in Figure 4a,c,d. As shown in Figure 4c, the differentiator output reproduces the temporal gradient of the input signal, consistent with the expected first-order derivative response. Feeding this output into the integrator reconstructs the original Gaussian pulse with only a slight temporal delay, as depicted in Figure 4d, thereby confirming the effective inverse operation of the cascaded pixel-MPU pair. Figure 4b,e shows the time-averaged surface electric-field intensity distributions at selected frequencies. The observed energy profiles at the output ports further validate that the inverse-designed metastructure kernels accurately realize the transfer characteristics required for differentiation and integration.

2.2 | Real-Time Image Encryption and Decryption With Dispersion-Engineered Pixel-MPUs

Building on the principle illustrated in Figure 1, real-time image encryption and decryption were implemented using cascaded integrator and differentiator pixel-MPUs, as shown in Figure 5. In this system, binarized images are first serialized into temporal pixel streams and amplitude-modulated (AM) into baseband analog signals through a digital-to-analog converter (DAC). These baseband signals are then upconverted in the analog domain by mixing with a $\cos(\omega_0 t)$ carrier to generate the waveforms that drive the pixel-MPUs. Though this experiment adopts a serial processing scheme, which may introduce latency for image data, our objective here is to demonstrate that integrator and differentiator units fabricated within the same pixelated platform can be cascaded to realize the full encryption-decryption process. Moreover, operating on 1D temporal signals provides a natural interface to existing analog front-end architectures. The integrator pixel-MPU serves as the encryption stage by blurring the image content, while the differentiator pixel-MPU functions as the decryption stage to reconstruct the original information by restoring edges and fine details. To emulate potential information-leakage scenarios, the blurred output of the integrator was additionally received and reconstructed using an SDR device. After downconversion and digitalization by an analog-to-digital converter (ADC), the recovered signal can be demodulated and restored into image form.

Two representative cases are presented: a composite Modified National Institute of Standards and Technology (MNIST) [48] digit image and a synthetic quick response (QR) code. For each case, the left panel shows the original binary image, the middle panel displays the blurred output after the integrator stage, and the right panel presents the reconstructed result following differentiation and demodulation. Notably, the recovered QR code can be successfully scanned and decoded by standard readers, whereas the blurred intermediate output remains unrecognizable, demonstrating effective obfuscation of visual information. Similarly, in the MNIST example, the blurred images cannot be correctly classified by the LeNet-5 network, while the reconstructed digits are identified with high confidence. These results confirm that the pixel-MPU-based analog computing architecture enables real-time, low-complexity encryption and decryption of image signals. The approach effectively conceals critical features during transmission while ensuring faithful recovery at the receiver, highlighting its potential for secure optical signal processing and lightweight data protection.

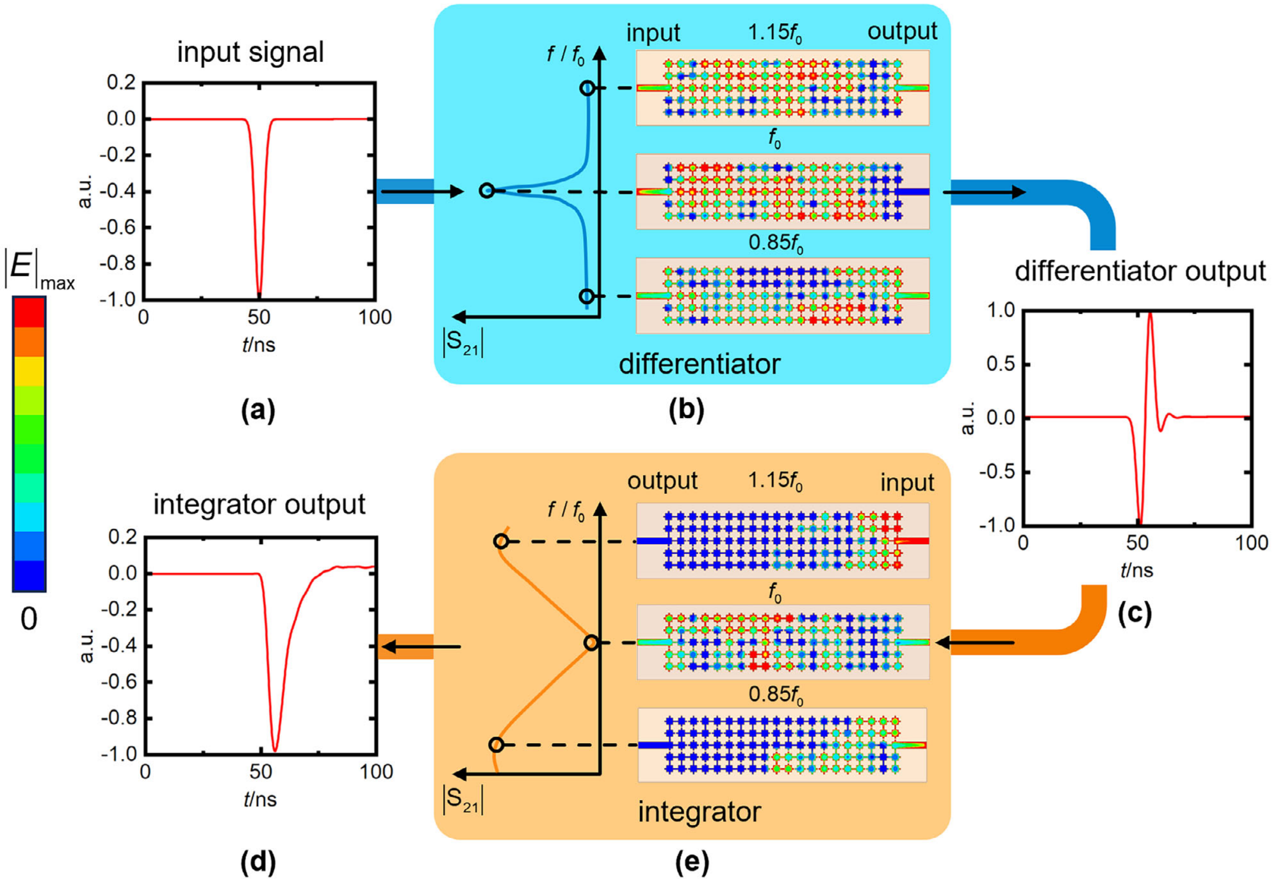

FIGURE 4 | Time-domain demonstration of differentiator and integrator pixel-MPUs. (a) The input Gaussian pulse signal. (b) Schematic of the dispersion-engineered differentiator pixel-MPU, together with the simulated surface electric-field distributions at representative frequencies ($0.85f_0$, f_0, and $1.15\ f_0$). (c) The output of the differentiator. (d) Reconstructed signal obtained after passing the differentiator output through the integrator pixel-MPU. (e) Schematic of the integrator pixel-MPU with corresponding surface electric field distributions.

TABLE 1 | Comparison of computational performance among different optical analog computation devices.

Reference	Method	Planar Structure	Size ($\lambda_0{}^2$)	CED
[18]	Pancharatnam-Berry Metasurface	No	5.6×10^6	7.4×10^{-8}
[45]	ENZ metamaterial	No	0.13	1.9
[51]	MZI array	Yes	1.2×10^3	2.3×10^{-7}
[52]	Coupled fiber	No	5.2×10^5	2.5×10^{-7}
[53]	Microring resonator	Yes	3.0×10^3	1.5×10^{-6}
[49]	Planar diffractive neural network	Yes	55.7	1.8×10^{-3}
[50]	Spoof plasmonic neural network	Yes	35.4	3.2×10^{-3}
Proposed	Pixel metastructure	Yes	0.087	2.9

Table 1 benchmarks our pixel-metastructure processor against representative optical computing platforms. In analog optical computing, the relative bandwidth is a critical performance indicator, as it determines how faithfully a device can process ultrafast, spectrally diverse signals without distortion. A narrowband processor may only function at a single carrier frequency or for spectrally confined inputs, whereas a broadband processor ensures robust operation across varying wavelengths, modulation formats, and application scenarios. To fairly compare heterogeneous photonic computing platforms across different spectral regimes, we therefore introduce a computational efficiency density (CED) as a dimensionless figure of merit that captures both spectral efficiency and device compactness:

$$\mathrm{CED} = \frac{\Delta f / f_0}{A/\lambda_0^2} \tag{3}$$

where $\Delta f / f_0$ is the relative bandwidth of the computing device (with Δf denoting the effective operation bandwidth and f_0 the center frequency), and A/λ_0^2 is the wavelength-normalized

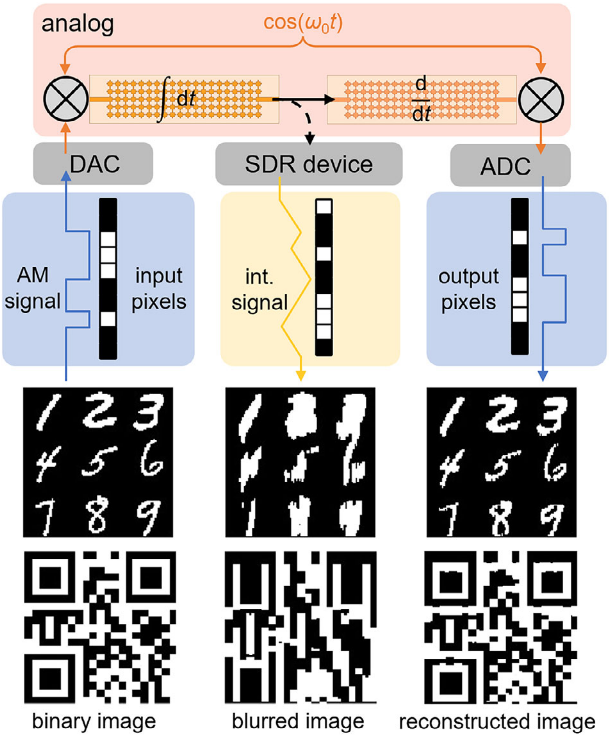

FIGURE 5 | Real-time image encryption and decryption using cascaded pixel-MPUs. Binary images are serialized into temporal signals, processed by an integrator pixel-MPU to generate blurred outputs, and subsequently restored by a differentiator pixel-MPU. Example images with MNIST digits and QR codes demonstrate that the original information can be effectively recovered.

device area (with A the physical footprint and λ_0 the free-space wavelength at f_0). This metric can be interpreted as the achievable relative bandwidth per wavelength-normalized unit area.

Prior photonic computing technologies either exhibit large wavelength-normalized footprints (10^3–10^6 $\lambda_0{}^2$) or suffer from narrow relative bandwidths (like MZI array), which in turn result in very low CED. Both the planar diffractive neural network [49] and the spoof plasmonic neural network [50] represent remarkable progress toward compact and CMOS-compatible platforms for analog electromagnetic computing. The planar diffractive neural network demonstrates a fully printed, conformal microwave implementation capable of direct in situ signal processing. The terahertz spoof plasmonic neural network further extends diffractive computing into the THz regime, leveraging surface-plasmonic coupling to realize even higher transmission efficiency and planar device compactness. It is also worth noting that several related works maintain broadly planar filtering structures, which helps simplify fabrication, reduce device complexity [49–53]. These two pioneering works provide valuable references for the development of dense and broadband metastructure computing platforms. The ENZ-MPU in [45] can achieve a much higher CED owing to its flexible subwavelength-scale tunable dispersion, but relies on complex 3D structures. In contrast, the proposed pixel-MPU, built on a fully planar and compact architecture, achieves the highest CED value and demonstrates clear advantages for high-density and broadband optical computing.

3 | Conclusion

In this work, we demonstrated a planar pixel-metastructure platform that emulates ENZ-inspired dispersion to implement subwavelength analog calculus operations, including the first realization of integral functionality within a planar pixelated structure. The architecture integrates an integrator–differentiator pair on the same platform, enabling seamless cascaded operations such as real-time analog image encryption and decryption, and we further provide the first systematic verification that such pixelated operators can jointly accomplish this encryption-decryption process. Through an improved optimization strategy—consisting of a MoM-based GA with physics-informed pathway initialization—we achieve solutions that are much closer to the global optimum rather than being trapped in local minima, thereby accelerating convergence and simultaneously improving key performance metrics such as operational bandwidth and in-band loss. Benefiting from these performance enhancements, the proposed 2D pixel-MPU achieves a significantly smaller footprint (0.58×0.15 $\lambda_0{}^2$), a wider operational bandwidth (>25%), and inherent planar fabrication compatibility compared with typical analog computation structures. Experimental characterization confirms the theoretical predictions, with measured S-parameters and time-domain responses matching simulations. We further introduce the computational efficiency density (CED) as a benchmark metric, under which the pixel-MPU exhibits state-of-the-art efficiency while maintaining integration-friendly planarity.

Beyond the demonstrated first-order differentiator-integrator pair, the proposed framework is intrinsically extensible to higher-order calculus operations. Simulations of 2nd-4th-order differentiator MPUs reproduce the desired transfer functions (shown in Figure S1), validating the scalability of the approach. Although prototypes were implemented at 1 GHz for fabrication and experiment convenience, the design principle is frequency-agnostic. Supporting simulations in Figure S2 show that geometrically scaled devices with minor optical-frequency adjustments yield the same transfer responses at 10 THz, confirming applicability in the optical domain.

While the present work targets binary-amplitude signals, future efforts will extend to grayscale and phase-encoded processing, integration with silicon photonics, and machine-learning-assisted inverse design. Overall, the proposed pixel-MPU establishes a compact, efficient, and scalable route toward high-density integrated analog computing, offering new opportunities for secure edge processing and low-power AI acceleration across frequency regimes.

4 | Methods

4.1 | Numerical Full-Wave Simulations

The numerical simulations on the 3D structure of pixel-MPUs have been carried out with ANSYS HFSS 23. The copper in the model is set as the perfect electric conductor (PEC) boundary condition. Two 50-ohm lumped ports are used to excite the SMA ports in the model. As shown in Figure 2a, we set the parameters as follows: $x = 20$, $y = 5$, $w_p = 4$ mm, $w_c = 0.8$ mm, $l_p = 1.2$ mm, $l_c =$

0.8 mm. All relative permittivity parameters are from the material library in the software.

4.2 | Optimization Methods

The optimization of the pixel-MPU is with GA, as shown in Figure 2. We use the optimization toolbox in MATLAB 2022b in this process. The parameters of GA for preliminary screening are: Generations = 5, PopulationSize = 2000, ParetoFraction = 0.2, CrossoverFraction = 0.5, MutationRate = 0.1. The parameters of GA for further screening are: Generations = 100, PopulationSize = 400, ParetoFraction = 0.2, CrossoverFraction = 0.7, MutationRate = 0.03. The fitness function at each iteration is defined as the linear correlation coefficient between the individual's computed dispersion curve and the desired target response. All optimizations run on a personal computer equipped with an Intel (R) Core (TM) i9-13900K CPU @ 3.00 GHz and random-access memory of 96.0 GB.

4.3 | Fabrication and Measurement Setup

The pixel-MPUs are fabricated using a printed circuit board (PCB) process, with 2 mm Rogers RO4350B dielectric with a relative dielectric constant of 3.66 and a loss tangent of 0.002. The vector network analyzer (KEYSIGHT FieldFox Microwave Analyzer N9951B 44 GHz) is used to measure the S-parameters of the pixel-MPUs.

4.4 | Time-Domain Signals

Based on the S-parameters measured with a vector network analyzer, we use MATLAB for time-domain analysis. We conduct a discrete Fourier transformation (DFT) on the input signal, then multiply it by the measured transmission parameters to obtain the frequency spectrum of the output signal, and subsequently carry out an inverse DFT to obtain the output time-domain signal. The Gaussian pulse signal used in the tests of Figure 4 has a duration of 100 ns and a −10 dB bandwidth of 180 MHz. The demodulation of the simulated leakage signal reconstruction in Figure 5 was performed using Otsu's thresholding method [54].

Acknowledgements

This work is supported by the National Key Research and Development Program of China under Grant No. 2021YFA0716601, the National Natural Science Foundation of China under Grant No. U22B2016, and the China National Postdoctoral Program for Innovative Talents under Grant No. BX20250350.

Conflicts of Interest

The authors declare no conflicts of interest.

Data Availability Statement

The data that support the findings of this study are available from the corresponding author upon reasonable request.

References

1. N. C. Thompson, K. Greenewald, K. Lee, and G. F. Manso, "The Computational Limits of Deep Learning," 2020, arXiv preprint arXiv:2007.05558 [cs.LG].

2. C. Silvano, D. Ielmini, F. Ferrandi, et al., *A Survey on Deep Learning Hardware Accelerators For Heterogeneous Hpc Platforms*, (ACM Computing Surveys, 2023).

3. Y. Wang, Y. Han, C. Wang, et al., "Computation-Efficient Deep Learning For Computer Vision: A Survey," *Cybernetics and Intelligence* (2024): 1–24.

4. B. R. Bartoldson, B. Kailkhura, and D. Blalock, "Compute-Efficient Deep Learning: Algorithmic Trends And Opportunities," *Journal of Machine Learning Research* 24, no. 122 (2023): 1–77.

5. W. Wang, D. T. Hoang, and P. Hu, , "A Survey On Consensus Mechanisms And Mining Strategy Management In Blockchain Networks," *IEEE Access* 7 (2019): 22328–22370, https://doi.org/10.1109/ACCESS.2019.2896108.

6. D. Mingxiao, M. Xiaofeng, Z. Zhe, et al., "A Review On Consensus Algorithm Of Blockchain," *IEEE International Conference on Systems, Man, and Cybernetics* 2017: 2567–2572.

7. A. Merlo, M. Migliardi, and L. Caviglione, "A Survey On Energy-Aware Security Mechanisms," *Pervasive and Mobile Computing* 24 (2015): 77–90, https://doi.org/10.1016/j.pmcj.2015.05.005.

8. P. He, Y. Zhou, and X. Qin, "A Survey On Energy-Aware Security Mechanisms For The Internet Of Things," *Future Internet* 16, no. 4 (2024): 128, https://doi.org/10.3390/fi16040128.

9. S. Sen, J. Koo, and S. Bagchi, "Trifecta: Security, Energy Efficiency, and Communication Capacity Comparison For Wireless Iot Devices," *IEEE Internet Computing* 22, no. 1 (2018): 74–81, https://doi.org/10.1109/MIC.2018.011581520.

10. P. L. McMahon, "The Physics Of Optical Computing," *Nature Reviews Physics* 5, no. 12 (2023): 717–734, https://doi.org/10.1038/s42254-023-00645-5.

11. H. J. Caulfield and S. Dolev, "Why Future Supercomputing Requires Optics," *Nature Photonics* 4, no. 5 (2010): 261–263, https://doi.org/10.1038/nphoton.2010.94.

12. D. R. Solli and B. Jalali, "Analog Optical Computing," *Nature Photonics* 9, no. 11 (2015): 704–706, https://doi.org/10.1038/nphoton.2015.208.

13. N. L. Kazanskiy, M. A. Butt, and S. N. Khonina, "Optical Computing: Status And Perspectives," *Nanomaterials* 12, no. 13 (2022): 2171, https://doi.org/10.3390/nano12132171.

14. K. Von Bieren, "Lens Design For Optical Fourier Transform Systems," *Applied Optics* 10, no. 12 (1971): 2739–2742, https://doi.org/10.1364/AO.10.002739.

15. J. Wu, X. Lin, Y. Guo, et al., "Analog Optical Computing For Artificial Intelligence," *Engineering* 10 (2022): 133–145, https://doi.org/10.1016/j.eng.2021.06.021.

16. X. Fang, X. Zheng, M. Li, Z. Li, and D. Ding, "Wireless Secure Communication Based On Code Domain Space-Time Modulated Metasurface," *Electromagnetic Science* 2, no. 4 (2024): 1–11, https://doi.org/10.23919/emsci.2024.0035.

17. Y. Chen, M. Nazhamaiti, H. Xu, et al., "All-Analog Photoelectronic Chip For High-Speed Vision Tasks," *Nature* 623, no. 7985 (2023): 48–57, https://doi.org/10.1038/s41586-023-06558-8.

18. X. Qiu, J. Zhang, Y. Fan, J. Zhou, L. Chen, and D. P. Tsai, "Metasurface Enabled High-Order Differentiator," *Nature Communications* 16, no. 1 (2025): 2437, https://doi.org/10.1038/s41467-025-57715-8.

19. J. Hu, D. Mengu, D. C. Tzarouchis, B. Edwards, N. Engheta, and A. Ozcan, "Diffractive Optical Computing In Free Space," *Nature Communications* 15, no. 1 (2024): 1525, https://doi.org/10.1038/s41467-024-45982-w.

20. H. H. Zhu, J. Zou, H. Zhang, et al., "Space-Efficient Optical Computing With An Integrated Chip Diffractive Neural Network," *Nature Communications* 13, no. 1 (2022): 1044, https://doi.org/10.1038/s41467-022-28702-0.

21. A. Silva, F. Monticone, G. Castaldi, V. Galdi, A. Alù, and N. Engheta, "Performing Mathematical Operations With Metamaterials," *Science* 343, no. 6167 (2014): 160–163, https://doi.org/10.1126/science.1242818.

22. R. Liang, S. Wang, Y. Dong, et al., "Metasurface-Generated Large And Arbitrary Analog Convolution Kernels For Accelerated Machine Vision," *ACS Photonics* 11, no. 12 (2024): 5430–5438, https://doi.org/10.1021/acsphotonics.4c01874.

23. J. Bueno, S. Maktoobi, L. Froehly, et al., "Reinforcement Learning In A Large-Scale Photonic Recurrent Neural Network," *Optica* 5, no. 6 (2018): 756–760, https://doi.org/10.1364/OPTICA.5.000756.

24. T. W. Hughes, I. A. D. Williamson, M. Minkov, and S. Fan, "Wave Physics As An Analog Recurrent Neural Network," *Science Advances* 5, no. 12 (2019): aay6946, https://doi.org/10.1126/sciadv.aay6946.

25. T. Yan, J. Wu, T. Zhou, et al., "Fourier-Space Diffractive Deep Neural Network," *Physical Review Letters* 123, no. 2 (2019): 023901, https://doi.org/10.1103/PhysRevLett.123.023901.

26. Y. Shen, N. C. Harris, S. Skirlo, et al., "Deep Learning With Coherent Nanophotonic Circuits," *Nature Photonics* 11, no. 7 (2017): 441–446, https://doi.org/10.1038/nphoton.2017.93.

27. R. Hamerly, L. Bernstein, A. Sludds, et al., "Large-Scale Optical Neural Networks Based On Photoelectric Multiplication," *Physical Review X* 9, no. 2 (2019): 021032, https://doi.org/10.1103/PhysRevX.9.021032.

28. H. Zhang, M. Gu, X. D. Jiang, et al., "An Optical Neural Chip For Implementing Complex-Valued Neural Network," *Nature Communications* 12, no. 1 (2021): 457, https://doi.org/10.1038/s41467-020-20719-7.

29. L. Wan, D. Pan, S. Yang, et al., "Optical Analog Computing Of Spatial Differentiation And Edge Detection With Dielectric Metasurfaces," *Optics Letters* 45, no. 7 (2020): 2070–2073, https://doi.org/10.1364/OL.386986.

30. Q. He, F. Zhang, M. Pu, et al., "Monolithic Metasurface Spatial Differentiator Enabled By Asymmetric Photonic Spin-Orbit Interactions," *Nanophotonics* 10, no. 1 (2020): 741–748, https://doi.org/10.1515/nanoph-2020-0366.

31. T. Zhu, Y. Zhou, Y. Lou, et al., "Plasmonic Computing Of Spatial Differentiation," *Nature Communications* 8, no. 1 (2017): 15391, https://doi.org/10.1038/ncomms15391.

32. P. Fu, Z. Xu, T. Zhou, et al., "Reconfigurable Metamaterial Processing Units That Solve Arbitrary Linear Calculus Equations," *Nature Communications* 15, no. 1 (2024): 6258, https://doi.org/10.1038/s41467-024-50483-x.

33. S. Shekhar, W. Bogaerts, L. Chrostowski, et al., "Roadmapping The Next Generation Of Silicon Photonics," *Nature Communications* 15, no. 1 (2024): 751, https://doi.org/10.1038/s41467-024-44750-0.

34. L. Ranno, P. Gupta, K. Gradkowski, et al., "Integrated Photonics Packaging: Challenges And Opportunities," *ACS Photonics* 9, no. 11 (2022): 3467–3485, https://doi.org/10.1021/acsphotonics.2c00891.

35. J.-H. Zheng, Q.-Q. Wang, L.-T. Feng, et al., "Global Calibration Of Large-Scale Photonic Integrated Circuits," *Physical Review Applied* 22, no. 5 (2024): 054011, https://doi.org/10.1103/PhysRevApplied.22.054011.

36. A. Marchisio, F. Da Ros, V. Curri, A. Carena, and P. Bardella, "Comprehensive Model Of Mzi-Based Circuits For Photonic Computing Applications," *Communications Physics* 8, no. 1 (2025): 277, https://doi.org/10.1038/s42005-025-02176-0.

37. I. Liberal and N. Engheta, "Near-Zero Refractive Index Photonics," *Nature Photonics* 11, no. 3 (2017): 149–158, https://doi.org/10.1038/nphoton.2017.13.

38. Y. Li, S. Kita, P. Muñoz, et al., "On-Chip Zero-Index Metamaterials," *Nature Photonics* 9, no. 11 (2015): 738–742, https://doi.org/10.1038/nphoton.2015.198.

39. P. Li, W. Yan, S. Wang, P. Fu, Y. Zhang, and Y. Li, "Engineering Epsilon-Near-Zero Media With Waveguides," *Advanced Physics Research* 3, no. 9 (2024): 2400070, https://doi.org/10.1002/apxr.202400070.

40. V. C. Nguyen, L. Chen, and K. Halterman, "Total Transmission And Total Reflection By Zero Index Metamaterials With Defects," *Physical Review Letters* 105, no. 23 (2010): 233908, https://doi.org/10.1103/PhysRevLett.105.233908.

41. Y. He, Y. Li, Z. Zhou, et al., "Wideband Epsilon-Near-Zero Supercoupling Control through Substrate-Integrated Impedance Surface," *Advanced Theory and Simulations* 2, no. 8 (2019): 1900059, https://doi.org/10.1002/adts.201900059.

42. M. Silveirinha and N. Engheta, "Design Of Matched Zero-Index Metamaterials Using Nonmagnetic Inclusions In Epsilon-Near-Zero Media," *Physical Review B—Condensed Matter and Materials Physics* 75, no. 7 (2007): 075119, https://doi.org/10.1103/PhysRevB.75.075119.

43. I. Liberal, A. M. Mahmoud, Y. Li, B. Edwards, and N. Engheta, "Photonic Doping Of Epsilon-Near-Zero Media," *Science* 355, no. 6329 (2017): 1058–1062, https://doi.org/10.1126/science.aal2672.

44. Z. Zhou, Y. Li, H. Li, W. Sun, I. Liberal, and N. Engheta, "Substrate-Integrated Photonic Doping For Near-Zero-Index Devices," *Nature Communications* 10, no. 1 (2019): 4132, https://doi.org/10.1038/s41467-019-12083-y.

45. H. Li, P. Fu, Z. Zhou, et al., "Performing Calculus With Epsilon-Near-Zero Metamaterials," *Science Advances* 8, no. 30 (2022): abq6198, https://doi.org/10.1126/sciadv.abq6198.

46. W. Yan, H. Li, X. Qin, et al., "Fano Resonance In Epsilon-Near-Zero Media," *Physical Review Letters* 133, no. 25 (2024): 256402, https://doi.org/10.1103/PhysRevLett.133.256402.

47. S. Song and R. D. Murch, "An Efficient Approach For Optimizing Frequency Reconfigurable Pixel Antennas Using Genetic Algorithms," *IEEE Transactions on Antennas and Propagation* 62, no. 2 (2013): 609–620, https://doi.org/10.1109/TAP.2013.2293509.

48. Y. Lecun, L. Bottou, Y. Bengio, and P. Haffner, "Gradient-Based Learning Applied To Document Recognition," *Proceedings of the IEEE* 86, no. 11 (2002): 2278–2324, https://doi.org/10.1109/5.726791.

49. Z. Gu, Q. Ma, X. Gao, J. W. You, and T. J. Cui, "Direct Electromagnetic Information Processing With Planar Diffractive Neural Network," *Science Advances* 10, no. 29 (2024): ado3937, https://doi.org/10.1126/sciadv.ado3937.

50. X. Gao, Z. Gu, Q. Ma, et al., "Terahertz Spoof Plasmonic Neural Network For Diffractive Information Recognition And Processing," *Nature Communications* 15, no. 1 (2024): 6686, https://doi.org/10.1038/s41467-024-51210-2.

51. W. Liu, M. Li, R. S. Guzzon, et al., "A Fully Reconfigurable Photonic Integrated Signal Processor," *Nature Photonics* 10, no. 3 (2016): 190–195, https://doi.org/10.1038/nphoton.2015.281.

52. M. Li, H.-S. Jeong, J. Azaña, and T.-J. Ahn, "25-Terahertz-Bandwidth All-Optical Temporal Differentiator," *Optics Express* 20, no. 27 (2012): 28273–28280, https://doi.org/10.1364/OE.20.028273.

53. X. Meng, N. Shi, G. Zhang, et al., "High-Integrated Photonic Tensor Core Utilizing High-Dimensional Lightwave And Microwave Multidomain Multiplexing," *Light: Science & Applications* 14, no. 1 (2025): 27, https://doi.org/10.1038/s41377-024-01706-9.

54. N. Otsu, "A Threshold Selection Method From Gray-Level Histograms," *Automatica* 11, no. 285-296 (1975): 23–27.

Supporting Information

Additional supporting information can be found online in the Supporting Information section.

Supporting File: lpor70750-sup-0001-SuppMat.docx